Partial discharge and interference discrimination in gas-insulated systems using electric and magnetic sensors

Mier Escurra, Christian; Mor, Armando Rodrigo ; Luo, Tianming; Vaessen, Peter

DOI
10.1016/j.ijepes.2024.109911

Publication date
2024

Document Version
Final published version

Published in
International Journal of Electrical Power & Energy Systems

Citation (APA)
Mier Escurra, C., Mor, A. R., Luo, T., & Vaessen, P. (2024). Partial discharge and interference discrimination in gas-insulated systems using electric and magnetic sensors. *International Journal of Electrical Power & Energy Systems*, *158*, Article 109911. https://doi.org/10.1016/j.ijepes.2024.109911

Electrical Power and Energy Systems 158 (2024) 109911

Contents lists available at ScienceDirect

International Journal of Electrical Power and Energy Systems

journal homepage: www.elsevier.com/locate/ijepes

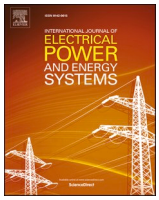

Partial discharge and interference discrimination in gas-insulated systems using electric and magnetic sensors

Christian Mier [a,*], Armando Rodrigo Mor [b], Tianming Luo [a], Peter Vaessen [a,c]

[a] Delft University of Technology, High Voltage Technology Group, Mekelweg 4, 2628 CD, Delft, the Netherlands
[b] Universitat Politècnica de València, Instituto de Tecnología Eléctrica, Camino de Vera s/n, 46022, Valencia, Spain
[c] KEMA Labs, Klingelbeekseweg 195, 6812 DE, Arnhem, the Netherlands

ARTICLE INFO

Keywords:
Partial discharges
Interference discrimination
Gas-insulated systems
Electric sensor
Magnetic sensor

ABSTRACT

The correct identification of partial discharges (PDs) is instrumental for the maintenance plan in gas-insulated systems (GIS). However, onsite PD measurements are difficult, especially in HVDC systems, where partial discharges can be confused with interference. This paper proposes a method to discern PDs from interferences based on the GIS characteristic impedance. The characteristic impedance is measured using very-high frequency electric and magnetic sensors, and it is calculated using four approaches based on the PD charge magnitude, peak value, peak-to-peak value, and frequency spectrum. The method is first tested with a PD calibrator in a matched and open-circuited GIS testbench. Then, the identification of PDs and interference is tested in a full-scale GIS, where the measurements are subjected to pulse overlapping and noise. Five types of interferences and PDs are injected into the GIS in two positions and measured in multiple mounting holes. The results show that all four approaches can precisely calculate the characteristic impedance in a matched testbench. In the full-scale GIS, these approaches show more deviation, with the peak approach being the most accurate. A practical application of the method is demonstrated using a calibrator in the full-scale GIS. The proposed method contributes to a more reliable PD monitoring system for HVDC/AC GIS and allows better maintenance planning, reducing unnecessary costs, notably for offshore substations.

1. Introduction

The increasing demand for offshore wind energy is one of the primary drivers of using gas-insulated systems (GIS). GIS offer a high reliability in a reduced space compared to traditional air-insulated systems, yet, GIS are subjected to insulation failures [1,2]. Partial discharge (PD) measurement is a powerful tool for electric insulation diagnosis [3,4] and is part of the IEC standard [5] for GIS commissioning. According to [5], the PD measurements must be in accordance to [6], but its implementation is complex in onsite substations where external noise (interference) is coupled. For that reason, [7] proposes unconventional PD measurement methods, where ultra-high frequency (UHF) antennas offer high noise rejection due to their operational frequency. However, interferences are coupled even at this frequency range, leading to false positive PD identification [8]. Therefore, discrimination of interference in online PD measurements is of interest and is critical for maintenance programs in remote places, such as offshore gas-insulated systems. For instance, in offshore GIS substations, a false positive identification of PDs leads to unnecessary and costly maintenance operations, that could be avoided with a better discrimination of real PDs and noise.

Partial discharges can be identified from interferences by software and hardware methods. Machine learning is a software method that has been gaining popularity recently. This tool uses clusters based on the PD characteristics [9,10,11], making it a powerful tool for not only filtering PDs from interference but also for classifying them. However, machine learning requires a massive database from previous discharges and many samples to correlate them with this database. Nevertheless, hardware methods do not require a pre-learning condition. The most recognized hardware method is the phase-resolve partial discharge method [12]. This method has proved very effective but requires an experienced technician and only applies to AC systems. Another hardware method in GIS is the discrimination of interference by an external antenna [13],

Abbreviations: GIS, gas-insulated system; PD, partial discharge; UHF, ultra-high frequency; VHF, very-high frequency; TEM, transverse electromagnetic; EM, electromagnetic; SNR, signal-to-noise ratio; FE, floating electrode; JP, jumping particle; CD, cavity discharge; FP, fast pulse.

* Corresponding author.
E-mail address: c.mierescurra@tudelft.nl (C. Mier).

https://doi.org/10.1016/j.ijepes.2024.109911
Received 11 October 2023; Received in revised form 19 January 2024; Accepted 28 February 2024

with the inconvenience of encompassing a short GIS length with multiple antennas.

This paper proposes a hardware discrimination method to distinguish between partial discharges and external interferences based on the estimation of an electromagnetic feature of a GIS. The procedure consists of calculating the GIS characteristic impedance via the electric and magnetic fields produced by the PD and measured with very-high frequency (VHF) electric and magnetic sensors. Any signal traveling in the GIS in the transverse electromagnetic (TEM) mode, such as partial discharges, has a fixed ratio between the electric and magnetic fields determined by the GIS characteristic impedance. On the contrary, external interferences coupled to the GIS don't propagate in TEM mode, inducing electric and magnetic fields with a different ratio.

The proposal for the characteristic impedance calculation is evaluated with four approaches in a matched testbench and a full-scale GIS. First, section 2 explains the principles of the electric and magnetic sensors in GIS, their relation to TEM mode waves, and their interaction with external interferences. Then, section 3 explains the four approaches based on the TEM characteristic impedance. Section 4 describes the sensors and the test setups used to verify the method. Section 5 gives the results and discussion of the experiments. Finally, section 6 describes a practical application of the presented method. The proposed method for partial discharge and external noise discrimination is a physically based method that mainly depends on the GIS geometry, hence, intrinsically independent of subjective operator interpretations.

2. Magnetic and electric sensors relation in the TEM mode

2.1. VHF electric and magnetic sensors

When PDs occur in a single-phase GIS, electromagnetic (EM) energy propagates as a coaxial waveguide. Maxwell's equations show that the wave propagates in 3 modes, depending on the frequency and the GIS geometry. The transverse electric and transverse magnetic modes only exist above certain cutoff frequencies, usually above the VHF range for GIS geometries. On the other hand, the transverse electromagnetic mode covers all frequency spectrum [1].

Fig. 1 shows a representation of the TEM propagation in a GIS, where the top half is represented by wave parameters and the bottom by voltage and current. The electric and magnetic fields in the TEM mode in a lossless media are related by the wave impedance $\eta = \sqrt{\mu/\varepsilon}$, as shown in (1), where μ and ε are the permeability and permittivity of the medium, $\boldsymbol{E}_\rho$ is the electric field in the radial direction, and $\boldsymbol{H}_\varphi$ is the magnetic field in the angular direction. The voltage ($\boldsymbol{V}$) and current ($\boldsymbol{I}$) can be found from the wave parameters using (2), where a and b are the GIS inner and outer conductor radius, r is the radial dimension, and l is the coaxial contour. The voltage and current ratio equals the characteristic impedance (Z_0), which is a physical constant that depends on the medium materials and geometry (3). Therefore, the characteristic impedance can be estimated by measuring the voltage and current with the corresponding sensors.

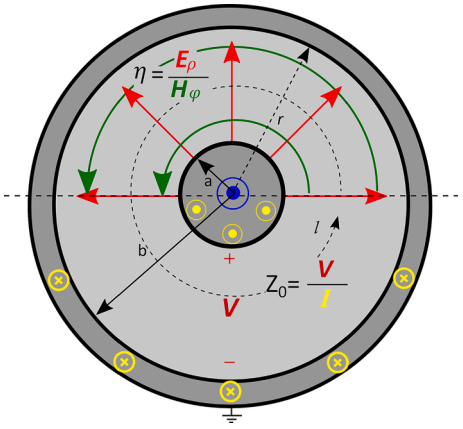

Fig. 1. TEM propagation in a GIS represented by wave parameters in the top half, and circuit parameters in the bottom half. The red arrows represent the electric field, the green arrows are the magnetic fields, the blue dot is the direction of propagation, and the yellow dots and crosses are the current. (For interpretation of the references to colour in this figure legend, the reader is referred to the web version of this article.)

$$\frac{\boldsymbol{E}_\rho}{\boldsymbol{H}_\varphi} = \eta \tag{1}$$

$$\boldsymbol{V} = \int_a^b \boldsymbol{E}_\rho(r)drand\boldsymbol{I} = \oint_0^{2\pi r} \boldsymbol{H}_\varphi(r)dl \tag{2}$$

$$\frac{\boldsymbol{V}}{\boldsymbol{I}} = Z_0 = \frac{\eta}{2\pi} ln(b/a) \tag{3}$$

Fig. 3 illustrates how the PD electromagnetic wave is sensed by an electric (grey disk) and a magnetic (orange loop) sensor placed in a GIS mounting hole[14,15]. On the one hand, the magnetic sensor couples the changing magnetic field produced by the PD current surrounding the mounting hole. On the other hand, the electric sensor (grey disk) couples the changing electric field produced by the PD voltage between the inner conductor and the sensor. Reference [15] shows the sensors' models for a frequency below 200 MHz, resulting in the Laplace-domain circuit in Fig. 2 and the electric (4) and magnetic (5) transfer functions. Where $\boldsymbol{V}_o$ is the sensors' output, $\boldsymbol{V}_{pd}$ and $\boldsymbol{I}_{pd}$ are the PD voltage and current, C_1 is the capacitive coupling of the electric sensor to the GIS inner conductor, C_2 is the capacitance from the sensor to the enclosure, M is the sensor's magnetic coupling, L is the sensor's self-inductance, and R is the sensors' load.

$$\boldsymbol{H}_e(s) = \frac{\boldsymbol{V}_{eo}(s)}{\boldsymbol{V}_{pd}(s)} = \frac{\boldsymbol{V}_{eo}(s)}{\boldsymbol{I}_{pd}(s)Z_0} = \frac{sC_1R}{sC_2R+1} whenf < 200MHzandC1 \ll C2 \tag{4}$$

$$\boldsymbol{H}_m(s) = \frac{\boldsymbol{V}_{mo}(s)}{\boldsymbol{I}_{pd}(s)} = \frac{sM}{sL/R+1} \ when\ f < 200\ MHz \tag{5}$$

Equations (4) and (5) demonstrate that the electric and magnetic sensors have the same transfer function with different constants. These parameters can be measured and calculated so one sensor can be scaled to the other [16]. By dividing (4) over (5), the magnetic sensor's transfer function can be scaled to the electric sensor, resulting in the scaling function $\boldsymbol{\alpha}_{e/m}$ in (6). Since the electric sensor measures the PD voltage and the magnetic sensor the PD current, the electric and scaled magnetic sensor outputs' quotient results in the GIS "local" characteristic impedance, as shown in (7). A GIS comprises multiple sections with different characteristic impedances, so the "local" Z_0 corresponds to the sensors' location. Equation (7) demonstrates that the estimated ratio of coaxial waves equals Z_0, and any other signal measured out of this TEM mode will give a different value. This fact, based on the physics of the propagation of a pulse in a coaxial structure, paves the way for PD and

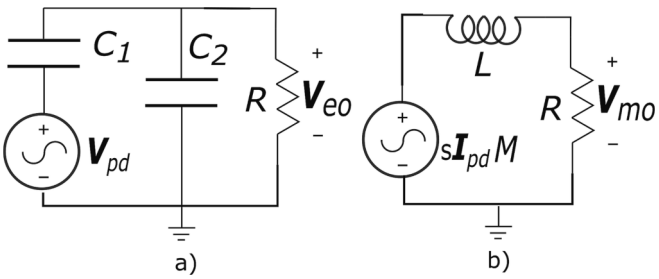

Fig. 2. a) electric and b) magnetic sensors' models up to 200 MHz, according to [15].

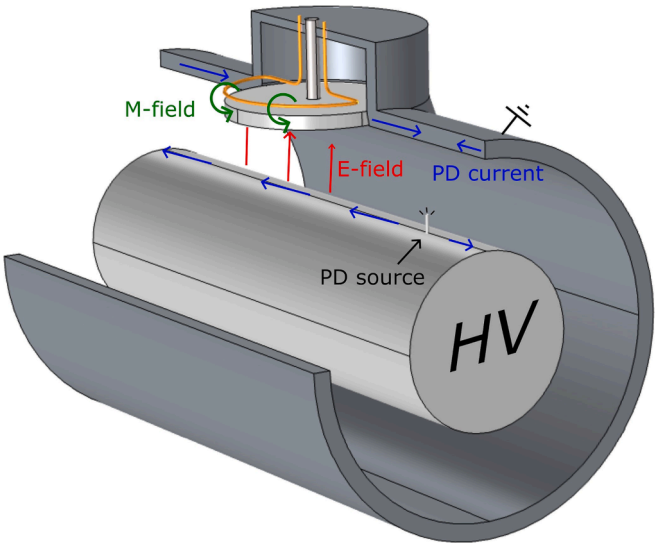

Fig. 3. PD magnetic and electric fields coupled to the magnetic (orange loop) and electric (grey disk) sensors. (For interpretation of the references to colour in this figure legend, the reader is referred to the web version of this article.)

external interference recognition.

$$\boldsymbol{\alpha}_{e/m}(s) = \frac{\boldsymbol{H}_e(s)}{\boldsymbol{H}_m(s)} = \frac{C_1 R(sL/R+1)}{M(sRC_2+1)} \tag{6}$$

$$Z_0 = \frac{\boldsymbol{V}_{pd}(s)}{\boldsymbol{I}_{pd}(s)} = \frac{\boldsymbol{V}_{eo}(s)/\boldsymbol{H}_e(s)}{\boldsymbol{V}_{mo}(s)/\boldsymbol{H}_m(s)} = \frac{\boldsymbol{V}_{eo}(s)}{\boldsymbol{V}_{mo}(s)\boldsymbol{\alpha}_{e/m}(s)} \tag{7}$$

2.2. Interference in a GIS

GIS substations are subjected to an uncountable number of transients and external interference. This interference is classified by frequency content, and duration [17]. The low-frequency transients are far from the PD sensors' bandwidth and are merely seen as a DC offset with a typical PD acquisition time in the range of microseconds. On the other hand, higher frequency impulse transients can be misidentified with partial discharges. The influence of these interferences on PD monitoring depends on the measuring system bandwidth and the PD-interference relative magnitude.

In this paper, the interferences are classified as conducted and external radiated interferences. The first ones originate in the power line and enter the GIS in the TEM mode. These interferences include the ones created by converters switching, corona discharges in the line, load switching, etc. The conducted interferences can be recognized by their propagation direction towards the GIS [8,18], as shown in Fig. 4. However, in the case of external radiated interference, the signal can arrive from any direction. Therefore, this paper focuses only on externally coupled interferences, such as the ones produced by radio communication, external electrostatic discharges, EM fields induced by near circuits, etc. Some examples of both interference channels are shown in Fig. 4.

The sensors' transfer functions shown in (4) and (5) are unique to the TEM mode. External interferences are not coupled to the GIS as a coaxial waveguide, resulting in different transfer functions for the sensors. Hence, the electric and magnetic ratio of external interference differs from those sensed in the coaxial TEM. The characteristic impedance calculated with the interference measurement leads to a value different from that of the GIS. Thus, it can be filtered out.

The following section presents four approaches to calculating the characteristic impedance based on different wave shape parameters. All the approaches use the measured signals from the electric and magnetic sensors.

2.3. Characteristic impedance calculation

The proposed method is based on the electric and magnetic sensors ratio. So, if the numerator and denominator are equally manipulated, the quotient (Z_0) will be unaltered. This section proposes four approaches to determine the characteristic impedance, having advantages and disadvantages in different situations.

2.3.1. Charge approach

Reference [19] demonstrates that derivative sensors can recover the PD charge, Q, by twice integrating its output voltage, V, and dividing over the coupling constant, k. The same reference demonstrates that to reduce the noise accumulation, the charge can be approximated by integrating up to the pulse second-zero crossing time (t_0), as shown in (8). By examining (8), it is noted that the coupling constant links the output voltage with the derivative of the PD current. This is the case of the magnetic sensor, where k equals M [Ωs]. On the contrary, the electric sensor's coupling constant associates the output voltage with the PD voltage derivative. Therefore, to estimate the PD charge using the electric sensor, the PD current is found by multiplying the coupling constant times the characteristic impedance, as shown in (4), resulting in k equal to $C_1 \bullet R \bullet Z_0$. Thus, the characteristic impedance results from dividing the electric and magnetic sensors' voltage double integral method, as shown in (9). The authors have demonstrated the charge estimation using electric and magnetic sensors in [15,16,20].

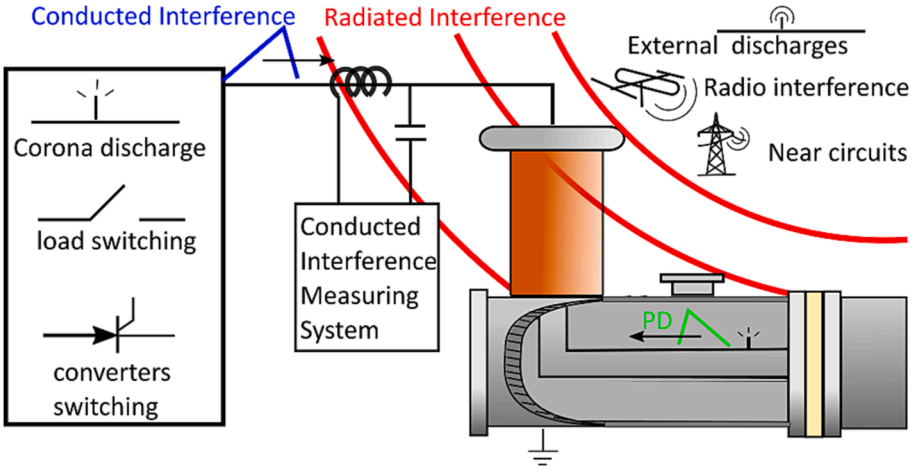

Fig. 4. Propagation of partial discharges and conducted and external interferences.

$$Q \approx \frac{1}{k}\int_0^{t_0}\int_0^{t_0} V_o(t)dtdt \tag{8}$$

$$\frac{M\int_0^{t_0}\int_0^{t_0} V_{eo}(t)dtdt}{C_1R\int_0^{t_0}\int_0^{t_0} V_{mo}(t)dtdt} \approx \frac{Q_eZ_0}{Q_m} \approx Z_0 \tag{9}$$

This approach only requires the coupling constant and does not rely on other electric parameters and the accuracy of the sensors' models. Nevertheless, this method is susceptible to noise and offset. Although the white noise should converge to zero as the pulse is integrated, the shift of the integration limits affects the measurements. The offset noise is the most critical since it is accumulated quadratically by the double integral [20]. The long integration time also affects the charge estimation due to the overlap of pulse reflections.

2.3.2. Peak approach

Another approach is to calculate the characteristic impedance with the electric and magnetic sensors' peak ratio. If a Dirac delta pulse with Q charge is measured with the sensors with transfer functions (4) and (5) and with a 1st-order low-pass filter, then the time-domain output voltage results in (10), where β equals Z_0 for the electric sensor and 1 for the magnetic sensor, [16]. This equation is valid only when the filter's cutoff frequency exceeds the sensors' one ($\omega_f > \omega_0$). By evaluating (10) for the magnetic and electric sensors' peak voltage, the ratio results in (11). If the electric and magnetic sensors have the same parameters by scaling with (6), then the ratio effectively equals the characteristic impedance (12). Unlike the charge method, the peaks depend on the self-inductance, the ground capacitance, and other high-frequency parasitic elements. Therefore, the measurement output must be processed with a high-order low-pass filter to avoid additional errors due to the disparity of the sensors.

$$V_o(t) = \frac{Q\beta k\omega_0\omega_f}{\omega_0 - \omega_f}\left(\omega_0 e^{-\omega_0 t} - \omega_f e^{-\omega_f t}\right) \tag{10}$$

$$\frac{V_{e-peak}}{V_{m-peak}} = \frac{Z_0C_1L}{MRC_2} \tag{11}$$

$$\frac{V_{e-peak}}{\alpha_{e/m}V_{m-peak}} = Z_0 \tag{12}$$

In addition to the sensors' high-frequency variation, the pulse peak is sensitive to the instrument's resolution and offset. The peak of a pulse changes when the time resolution is not big enough. Therefore, data acquisition must have the highest sampling rate, which adds additional cost to the equipment. The quantization error becomes important for low-resolution equipment. Equation (13) shows the quantification error, ε, where a is the proportion of the peak with the vertical scale, and n is the number of bits. The number 2 at the numerator corresponds to the worst case when one sensor rounds up and the other rounds down the quantization level. PD magnitude variation leads to overscaling the vertical scale to avoid clipping. So, with a peak value four times smaller than the vertical scale and with an 8-bit resolution, the error can be as high as 1.6 %. A more significant error source is the offset that can shift the peak value.

$$\varepsilon \le \frac{2}{a2^{n+1}} \tag{13}$$

2.3.3. Peak-peak approach

The narrow-band response of the sensors results in a pulse with a huge undershoot [19]. The incident peak and undershoot peak subtraction eliminates the measured offset. This approach removes the offset and is less affected by noise since it has a larger signal-to-noise ratio. However, the undershoots peak requires more measuring time, where a reflection may overlap. Like the incident peak method, the peak-to-peak depends on all the sensors' parameters. Since this method requires two quantities for each sensor, the quantification error can be twice that of the previous approach.

2.3.4. Frequency approach

Another way to find the characteristic impedance is by evaluating the sensors' frequency response ratio in (7). The evaluation of a single frequency becomes too sensitive to noise, so we propose integrating the absolute value in a frequency range (f_1 to f_2), resulting in (14). The white noise has a normal distribution, meaning that its integration in the time or frequency domain approximates zero. Additionally, the low-frequency noises, responsible for the offset error, can be rejected by increasing the lower integration limit. This method shows the highest noise immunity; however, the estimation of the characteristic impedance depends on the sensor's scalation and the frequency range.

$$\frac{\int_{f_1}^{f_2} |\boldsymbol{V}_{eo}(2\pi f)|df}{\int_{f_1}^{f_2} \left|\boldsymbol{\alpha}_{e/m}(2\pi f)\boldsymbol{V}_{mo}(2\pi f)\right|df} = Z_0 \tag{14}$$

When a noiseless GIS is matched, (14) gives the characteristic impedance irrespective of the integration limits. Nevertheless, a discontinuity near the observation point affects the Z_0 calculation. The voltage and current in a GIS can be modelled with the transmission line equations (15) and (16), where z is the distance of the observation point to a discontinuity, $\boldsymbol{V}^+$ is the voltage forward propagation, and c is the speed of light. Assuming that the discontinuity is a bushing with a high impedance, the measured voltage and current with the electric and magnetic sensors can be simplified as (17) and (18), respectively. Therefore, substituting (17) and (18) into (14) results in Fig. 5, where φ is the ratio of the transmission line length and the wavelength ($\varphi = 2\pi fz/c$), and $Z(\varphi)$ is the estimated characteristic impedance. Two conclusions can be extracted from this result:

- The wider the integration limits are, the better $Z(\varphi)$ approaches Z_0
- If the discontinuity is too close to the measuring point, $Z(\varphi)$ takes longer to converge.

Hence, the best results are obtained by covering a wide frequency range. Nevertheless, at a higher frequency, the electric and magnetic sensors' models deviate.

$$\boldsymbol{V} = \boldsymbol{V}^+\left(e^{-\frac{j2\pi fz}{c}} + \tau e^{\frac{j2\pi fz}{c}}\right) \tag{15}$$

$$\boldsymbol{I} = \frac{\boldsymbol{V}^+}{Z_0}\left(e^{-\frac{j2\pi fz}{c}} - \tau e^{\frac{j2\pi fz}{c}}\right) \tag{16}$$

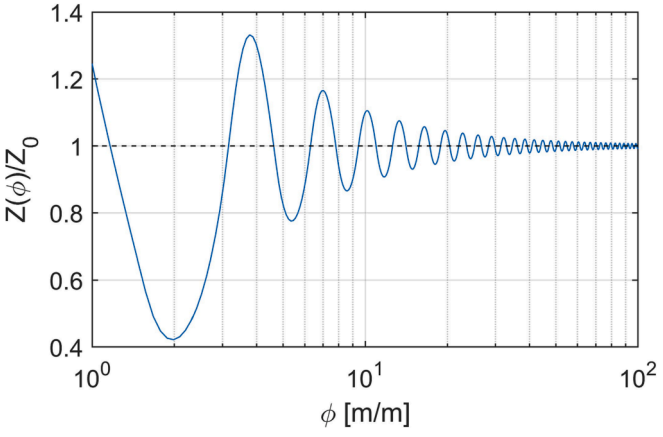

Fig. 5. Characteristic impedance approximation as the discontinuity distance and/or wavelength ratio increases.

$$\boldsymbol{V}_{eo} = 2\boldsymbol{H}_e\boldsymbol{V}^{+}\cos\left(\frac{2\pi fz}{c}\right) \tag{17}$$

$$\boldsymbol{V}_{mo} = \frac{-j2\boldsymbol{H}_m\boldsymbol{V}^{+}}{Z_0}sin\left(\frac{2\pi fz}{c}\right) \tag{18}$$

2.4. Summary

This section presented four approaches to calculate the local characteristic impedance. Each one uses a different parameter of the measured pulse, leading to the advantages (green) and disadvantages (red) shown in Table 1. The error sources mainly depend on the signal-to-noise ratio (SNR), the relative distance of the sensor and discontinuities, and the deviation of the sensors' models. Fig. 6 exemplifies the different pulse times required for each method, which affect the result due to the pulse overlapping.

3. Test setups

The proposed method is investigated using a matched testbench and a full-scale GIS. On the one hand, the matched testbench evaluates an ideal situation with low noise and without reflections. On the other hand, the full-scale GIS setup is subjected to multiple discontinuities and noise, giving different errors for each discrimination method. In both test setups, the electric and magnetic sensors share a common mounting hole.

3.1. Sensors

The electromagnetic field can be measured by placing both sensors in the same transversal position, either by different mounting holes or sharing the same one. The last option has the advantage that only one mounting hole is required. Still, in this research, the reason for choosing a single hole is to demonstrate that the interference is induced differently in the electric and magnetic couplers, even when placed in the same location. Fig. 7 shows the electric and magnetic sensors used with their dimensions indicated. The aluminium plate with a carbon black-epoxy rim is the electric coupler, and below, the magnetic coupler consists of a balanced loop [21]. Each sensor has its output, so the electric and magnetic sensor signals are measured individually.

3.2. Matched testbench

To prove that the electric and magnetic sensors' ratio is the characteristic impedance, the testbench in Fig. 8 was used. The testbench consists of a TEM chamber where a pulse is injected in one of the transition cones, measured with the couplers in the middle section, and terminated in the second transition cone. The methods are first tested in a fully-matched 50 Ω setup, and then with an open termination. In the open-circuit case, the pulse is reflected, affecting the measured characteristic impedance.

Table 1
Advantages and disadvantages of the four approaches to calculate the characteristic impedance.

	Charge	Peak	Peak-peak	Frequency
Sensors parameters	Calibration constant	All parameters	All parameters	All parameters
White noise	Heavily affected	StdDev affected	StdDev affected	Not affected
Offset noise	Heavily affected	Affected linearly	Not affected	Slightly affected
Reflections	Heavily affected	Less affected	Affected	Heavily affected
Resolution	Slightly affected	More affected	More affected	Not affected
Frequency content	Not affected	Affected	Affected	Highly affected

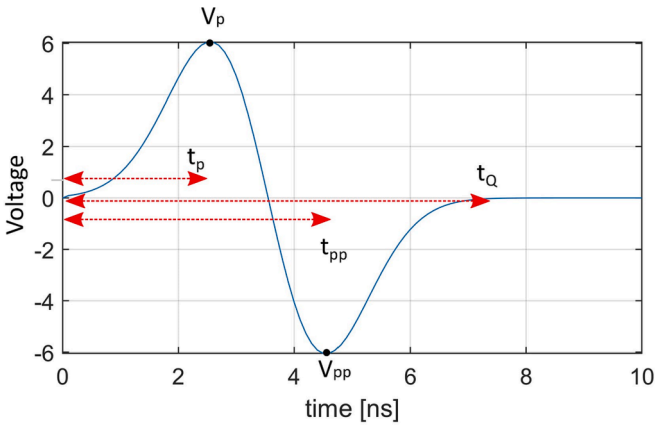

Fig. 6. Pulse times required for the peak method (t_p), peak-peak method (t_{pp}), and charge method (t_Q).

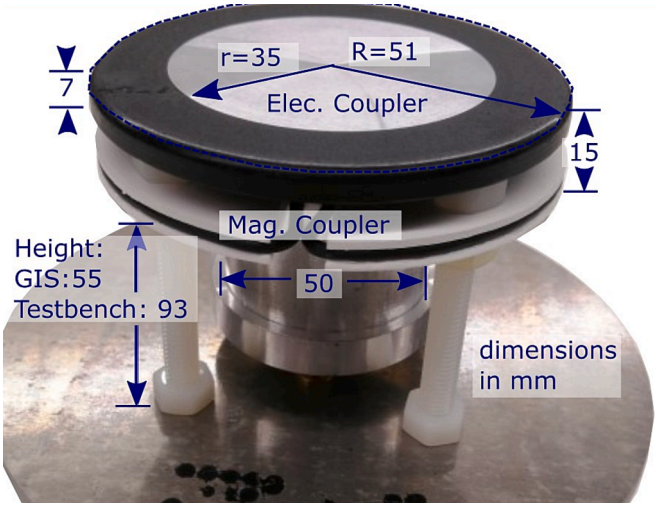

Fig. 7. Picture and dimensions of the electric and magnetic sensors used for the tests.

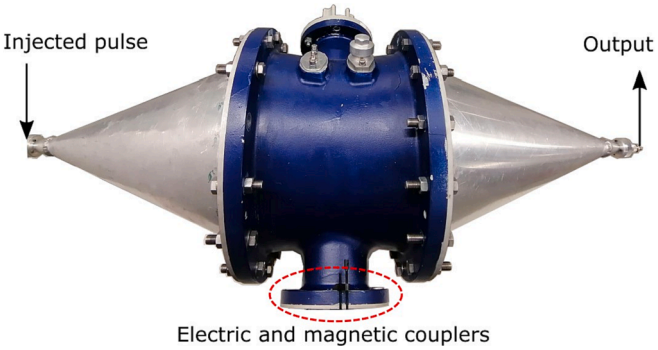

Fig. 8. Testbench used to test the methods in a matched case and open-circuited.

3.3. Full-scale GIS

The discrimination between PD pulses and interference is tested in the full-scale GIS illustrated in Fig. 9.

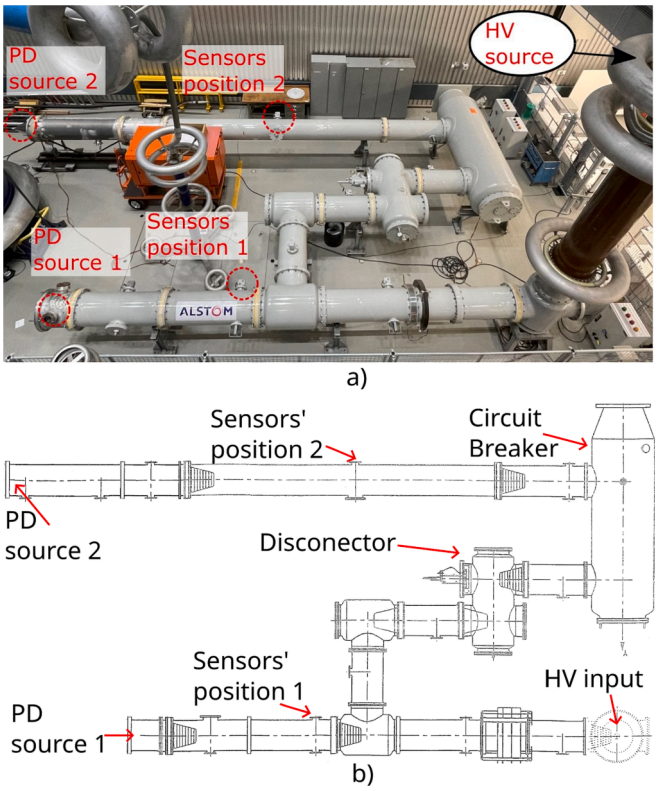

Fig. 9. Full-scaled GIS a) picture and diagram b) used to discriminate PDs and interferences.

Unlike the TEM chamber, the full-scale GIS comprises multiple discontinuities such as spacers, disconnectors, T-sections, bushings, etc., which cause multiple reflections. In addition to the reflections, the small PD magnitude results in measurements with lower SNR. In this test, the PDs and the interferences were measured in two locations in the GIS. In position 1, the sensors were located next to a T-section, where 1/3 of the propagated wave is reflected, as shown in [22]. In position 2, the sensors are distanced from any discontinuity, like in the case of a gas-insulated line. The PDs were also introduced in two locations with different propagation paths to the sensors.

The PD defects used in this research were a floating electrode (FE), jumping/moving particle (JP), cavity discharge (CD), surface discharge (SD), and protrusion (Cor), each of them having a different discharge mechanism. In addition to the defects, a fast-pulse calibrator (FP) was also used. These defects were placed in both positions for each sensor's locations to measure both PD directions. The corona and surface discharges were omitted for the defect located opposite the sensors because the signal is lost due to the attenuation along the GIS. For both sensors' locations, different interferences were injected.

Five interferences were coupled to the GIS and measured with the sensors. A current loop between the laboratory ground mesh and the GIS enclosure was injected with a fast-pulse calibrator (E2Gn), inducing a magnetic field and a potential difference in the sensors' mounting hole. Electromagnetic fields were generated with a log-periodic antenna fed with a Haefely USG 40 generator (TV) and a floating electrode discharged in the laboratory ground mesh (FEEM), inducing noise in the sensors' coaxial cables connected to the GIS structure [24]. Another interference source was an external floating electrode discharged in the enclosure of the GIS (FEE). The last interference was an external magnetic field produced by a nearby motor fed with a variable frequency driver (motor). Since none of these interferences are coupled to the sensors in the coaxial TEM mode, the ratio is expected to result in a distinct result from the GIS characteristic impedance.

3.4. Measuring system

Fig. 10 illustrates the measuring system used for the testbench and the full-scale GIS. The sensors' outputs were connected to amplifiers depending on the signal intensity. For the corona and surface discharge, the calibrator pulse, and all interferences, the electric and magnetic sensors were connected to 25 dB and 28.8 dB ZFL-500 Mini-Circuits amplifiers, respectively. In the case of the testbench, 30 dB gain amplifiers were used for both sensors. Then, at the oscilloscope's input, the signal was filtered with 200 MHz and 100 MHz 8th-order low-pass filters for the testbench and 200 MHz and 50 MHz for the full-scale GIS. In parallel with the filters and the oscilloscope, surge arresters with a 100 MHz low-pass filter response were used in the full-scale GIS scenario. The oscilloscope consisted of a Tektronix MSO58 with 2 GHz bandwidth and a sample rate of 6.25 GS/s.

4. Results and discussions

4.1. Matched testbench

Table 2 shows the testbench's calculated characteristic impedance when matched and open-circuited. In the matched case, the results are very close to the characteristic impedance of 50 Ω. The peak, peak-peak, and frequency method results are improved with the 100 MHz filter because the sensors' parameters are better approximated at low frequencies. In the case of the charge method without discontinuities, the filter does not affect the result.

The characteristic impedance is accurately calculated if the waveguide has no discontinuities close enough to the sensors, leading to an overlapped measurement. When the testbench is open-circuited, different characteristic impedances are obtained for each method because the overlapping increases with the pulse progression. For instance, the peak method at 200 MHz is less affected because the reflection does meet the incident pulse peak. When the sensors are filtered with 100 MHz, the pulse is slower, and the reflection overlaps with the incident pulse peak. This extreme case of discontinuity shows its effect on the characteristic impedance calculation.

4.2. Full-scale GIS

In the previous test setup, the characteristic impedance was calculated to show the testbench's 50 Ω. In the full-scale GIS, the geometry changes in every section, giving a different local characteristic impedance. Hence, it is more convenient to normalize the sensors' ratio. For that, the electric sensor's coupling factor must be multiplied by the local characteristic impedance, which is known in advance with the GIS geometry (3). With this normalization, the sensors' ratios of TEM signals are expected to approximate to one.

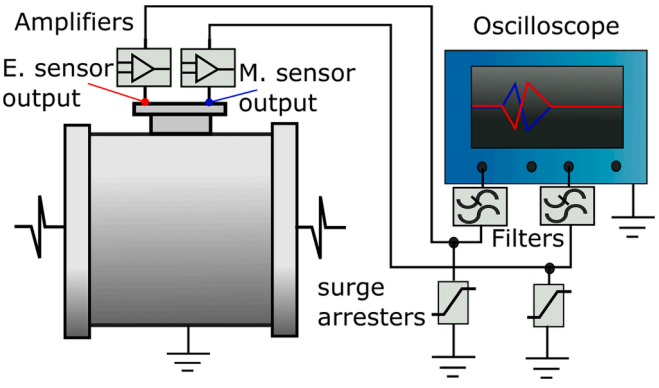

Fig. 10. Measuring system used for the testbench and the full-scale GIS. The surge arresters were not used in the testbench.

Table 2
Calculated characteristic impedance for a matched and open-circuited testbench [25].

	Charge	Peak	Peak-Peak	Frequency
Mat. @200 MHz	49.0 Ω	52.4 Ω	52.7 Ω	51.9 Ω
Mat. @100 MHz	48.9 Ω	50.5 Ω	50.3 Ω	49.4 Ω
OC @200 MHz	61.7 Ω	52.6 Ω	22.4 Ω	35.2 Ω
OC @100 MHz	46.1 Ω	60.2 Ω	33.9 Ω	33.1 Ω

Fig. 11 shows the cluster of the magnetic and electric outputs of 1700 PD and interference samples. The cluster corresponds to the peak's approach when the sensors and the defects are in the second location and with the 200 MHz low-pass filter. In this result, the PDs are close to the unit slope, and the interferences give a different ratio. When the SNR decreases, the results have more dispersion for each type of signal. This can be seen in Fig. 11: as the signal magnitude decreases, the electric and magnetic measurements lose the linearity between them. This clear clustering is not obtained in every sensor position, discrimination method, and filtering, as shown in Figs. 12–15 and Tables 3–6.

The results are presented in four scenarios. In the first two situations, the sensors are located in position "1″ and filtered at 200 and 50 MHz. Using the same filters, in the following two scenarios the sensors are located in position "2". In each situation, all the interferences ratios are compared with the PDs source in the two locations, displayed as a bar plot. The results of each approach are presented in a confusion matrix where the ratios inside the 0.8–1.2 range are considered PDs, and everything outside this range is considered interference. In this matrix, the true positives are the correct PDs, the true negatives are the correct interferences, the false negatives are incorrect PDs, and the false positives are incorrect interferences. These tables evaluate two standard deviations of each defect and interference above 5 pC (omitting corona discharge and motor interference). This 5 pC value is based on the CIGRE recommendation of the maximum allowed charge for GIS [26].

Fig. 12 and Fig. 13 show the results for location 1. In this location close to a discontinuity, the incident pulse length is critical, which depends on the filter used. The PDs and interferences ratios overlap, giving a high proportion of false positives and negatives, as shown in Table 3 and Table 4. The high error is attributed to the T-section discontinuity that affects the slow pulses. The 50 MHz low-pass filter gives longer pulses with lower magnitude, showing a worse result. Considering that it is more important to find true PDs than interferences, the Peaks' ratio

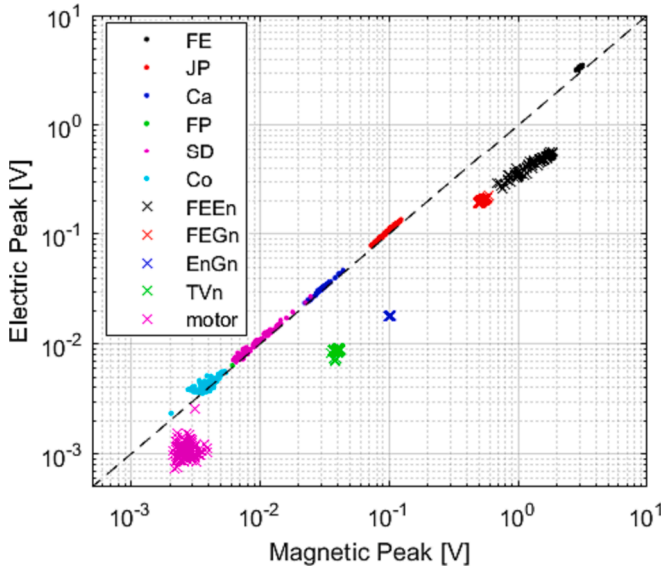

Fig. 11. Cluster of the PDs and interferences using the peak approach in the sensors' position 2 with a 200 MHz filter [25].

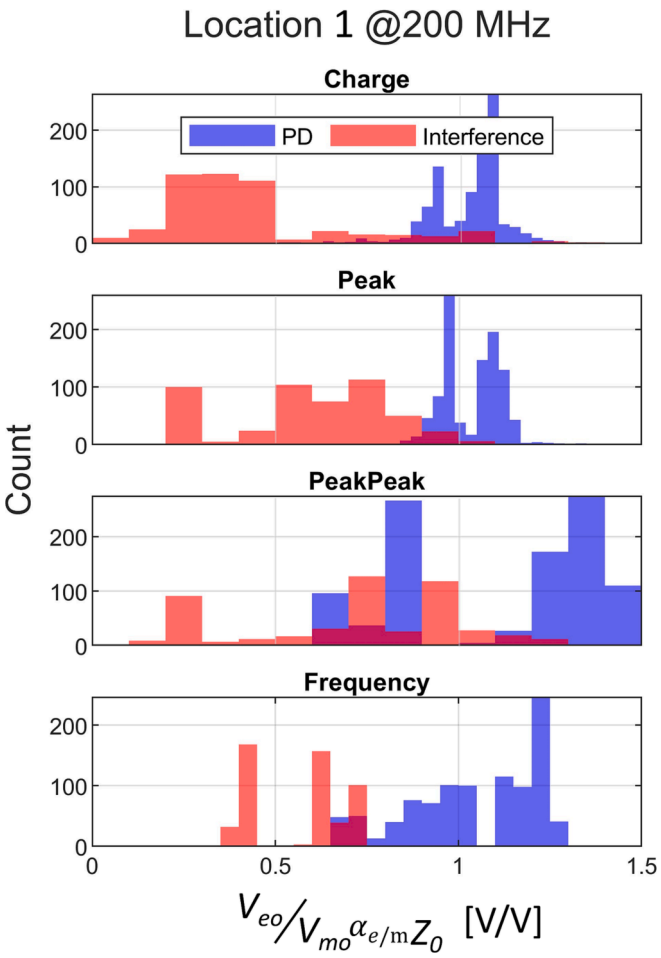

Fig. 12. Ratios count for each approach for sensor position 1 using 200 MHz filters [25].

gave the best results with 99 % accuracy for signals above 5 pC.

The results are improved for location 2 with no discontinuities in both propagation directions, as shown in Fig. 14, Fig. 15, Table 5, and Table 6. In the case of the 200 MHz filter, PDs and interferences for all methods have no overlap. However, due to the short range for the PD threshold, only the Peak method is above 95 %. When the 50 MHz filter is used, accuracy is lost for the measurements below 5 pC because of the decrease in signal-to-noise ratio. According to the results, increasing the PD threshold in a GIS without discontinuities is more convenient. Still, when the sensor is close to a discontinuity, the high dispersion of PDs and interference narrows the threshold to avoid false positives.

The different approaches for the proposed method can be used depending on the situation. For example, the charge method is a good option in a GIL application when the measuring system has a low bandwidth and resolution. In the case of a noisy measuring system, the frequency method offers a good solution. However, the peak method was the most versatile, having the best results for all kinds of situations.

The low-pass filter selection showed an important influence on the results. On one hand, a high cutoff frequency decreases the pulse overlapping and increases the SNR. On the other hand, the magnetic and electric sensors' frequency responses diverge at higher frequencies, which is more complex to predict. This creates a spread of the results since each type of PD has a different response at this frequency range (>30 MHz), [23]. Overall, the interference discrimination method proved to work, but higher accuracy can be achieved by improving the sensors' design.

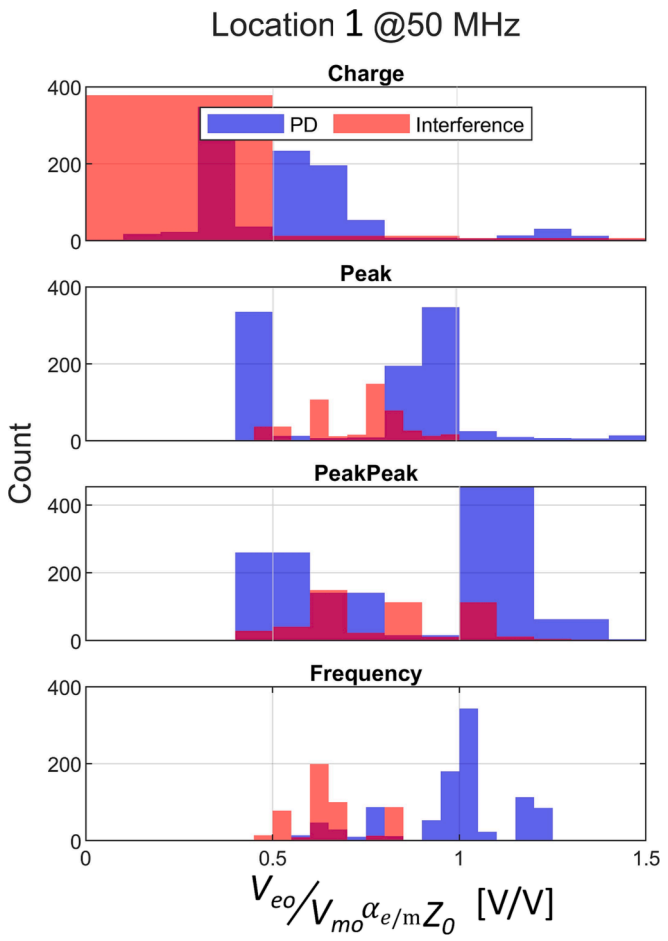

Fig. 13. Ratios count for each approach for sensor position 1 and 50 MHz filter [25].

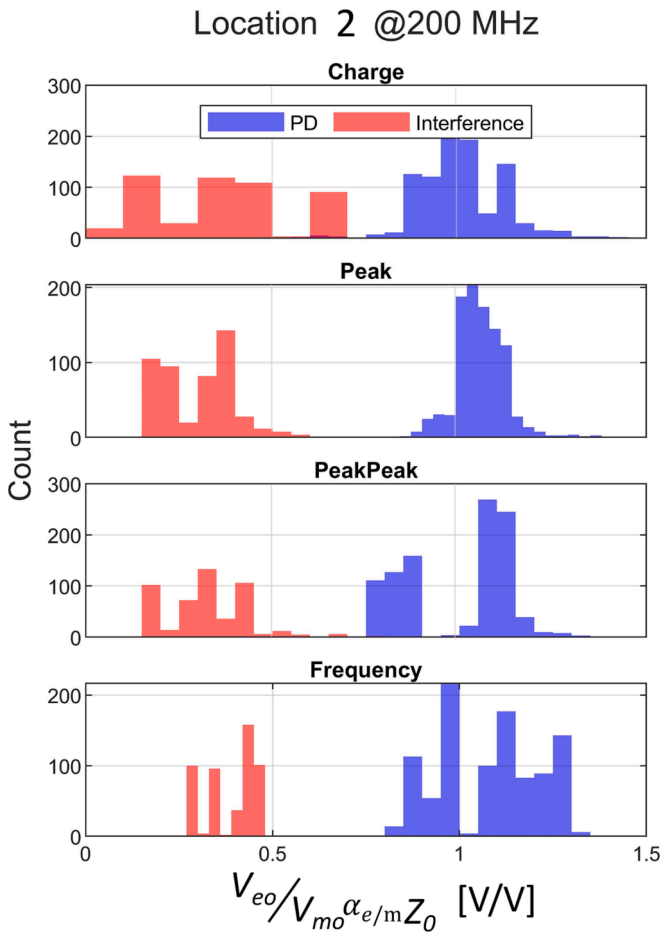

Fig. 14. Ratios count for each approach for sensor position 2 using 200 MHz filters [25].

5. Practical application

Regarding the practical application of the method, it is worth noticing that it works even when the sensors' parameters are unknown. In this case, the ratio of the measurements will not lead to the GIS characteristic impedance but will result in a constant ratio for all TEM propagation. This constant can be found with a calibrator injecting a signal in TEM mode. For instance, Fig. 16 is a replica of Fig. 11 but without scaling the sensors, assigning an arbitrary value of 1 to all parameters (M, C_1, C_2, L, Z_0, R). The slope is calculated with the calibrator's measurement and is used as the reference for the interference discrimination threshold. This is a practical application of the presented method based on the TEM propagation physics.

6. Conclusions

The presented research demonstrates that partial discharges can be discerned from external interference by measuring the GIS characteristic impedance with electric and magnetic couplers. The method is based on a physical property (GIS' characteristic impedance) invariable of any other parameters and was validated with four different approaches: charges, peaks, peak-peak, and frequency domain.

The following was concluded from the results:

- In a low noise and no reflection testbench, the method probes to work with an error below 5 % for all approaches.
- Each approach gave different results in a full-scale GIS, depending on the propagation reflections and the SNR.
- The best PD and interference segregation was obtained with the peaks approach, identifying 98 % of the PD and 100 % of interference.
- A calibrator can be used instead of the sensors' parameters as a practical application of the proposed method.

The method's main error source is attributed to the inaccuracy of the sensors' models at higher frequencies. Therefore, the results can be improved with the electric and magnetic sensors' design. These findings are an important contribution to the rapidly increasing demand for HVDC GIS, enabling the correct assessment of maintenance needs.

CRediT authorship contribution statement

Christian Mier: Writing – review & editing, Writing – original draft, Visualization, Methodology, Investigation, Formal analysis, Conceptualization. **Armando Rodrigo Mor:** Writing – review & editing, Supervision, Project administration, Conceptualization. **Tianming Luo:** Methodology. **Peter Vaessen:** Writing – review & editing, Project administration.

Declaration of competing interest

The authors declare that they have no known competing financial interests or personal relationships that could have appeared to influence the work reported in this paper.

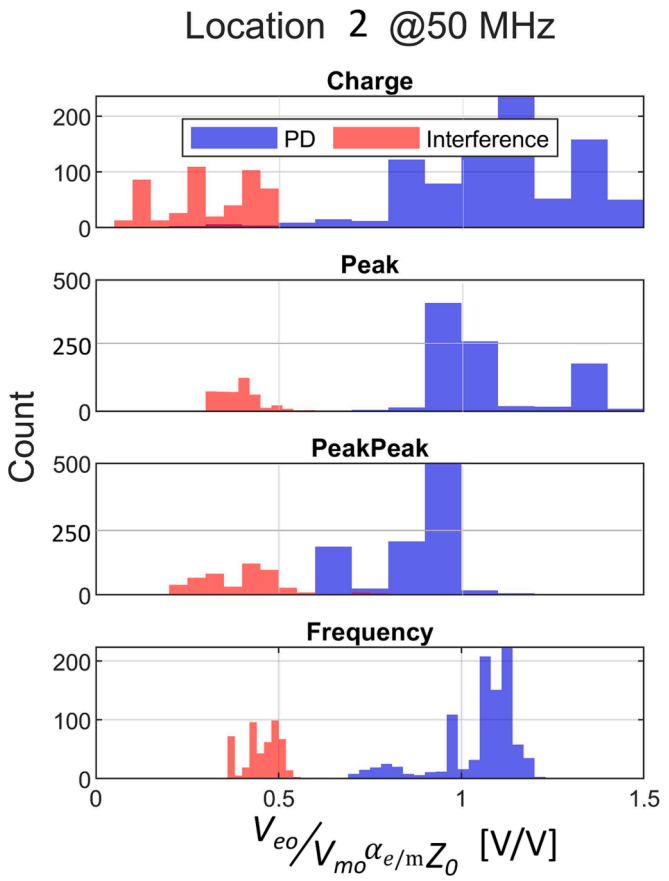

Fig. 15. Ratios count for each approach for sensor position 2 and using 50 MHz filters [25].

Table 3
Confusion matrix with a 0.8–1.2 threshold for the 4 approaches in position 1 using 200 MHz filters [25].

Loc.1 @200 MHz	Charge	Peak	Peak-peak	Freq.
True positive	95 %	99 %	30 %	60 %
False negative	5 %	1 %	70 %	40 %
True negative	90 %	85 %	61 %	100 %
False positive	10 %	15 %	39 %	0 %

Table 4
Confusion matrix with a 0.8–1.2 threshold for the 4 approaches in position 1 using 50 MHz filters [25].

Loc.1 @50 MHz	Charge	Peak	Peak-peak	Freq.
True positive	3 %	58 %	47 %	72 %
False negative	97 %	42 %	53 %	28 %
True negative	99 %	72 %	49 %	82 %
False positive	1 %	28 %	51 %	18 %

Table 5
Confusion matrix with a 0.8–1.2 threshold for the 4 approaches in position 2 using 200 MHz filters [25].

Loc.2 @200 MHz	Charge	Peak	Peak-peak	Freq.
True positive	94 %	98 %	87 %	76 %
False negative	6 %	2 %	13 %	24 %
True negative	100 %	100 %	100 %	100 %
False positive	0 %	0 %	0 %	0 %

Table 6
Confusion matrix with a 0.8–1.2 threshold for the 4 approaches in position 2 using 50 MHz filters [25].

Loc.2 @50 MHz	Charge	Peak	Peak-peak	Freq.
True positive	64 %	74 %	75 %	93 %
False negative	36 %	26 %	25 %	7 %
True negative	100 %	100 %	100 %	100 %
False positive	0 %	0 %	0 %	0 %

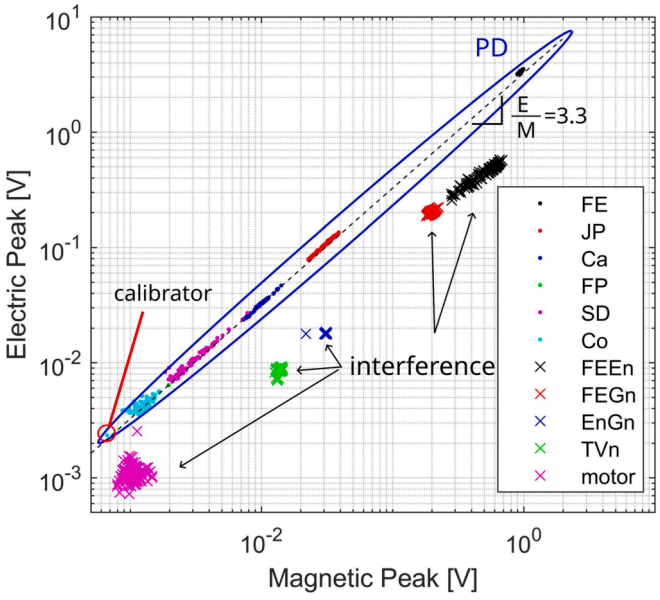

Fig. 16. Same cluster as Fig. 11 but without scaling the sensors.

Data availability

The dataset is available in a open access repositorium and is referenced in the paper.

Acknowledgements

This project 19ENG02 FutureEnergy has received funding from the EMPIR programme co-financed by the Participating States and from the European Unions Horizon 2020 research and innovation programme. Funder ID: 10.13039/100014132.

References

[1] Darwish A, Refaat SS, Toliyat HA, Abu-Rub H. On the electromagnetic wave behavior due to partial discharge in gas insulated switchgears: State-of-art review. IEEE Access 2019;7:75822–36.
[2] Aaradhi V, Gaidhani K. "Partial discharge in Gas Insulated substations (GIS): A development and engineering perspective". 12th Int Conf Environ Electr Eng EEEIC 2013;2013:112–7.
[3] IEC, "IEC 60885-3: Test methods for partial discharge measurements on lengths of extruded power cables," 2015.
[4] W.G. D1.25, "UHF partial discharge detection system for GIS: Application guide for sensitivity verification," 2016.
[5] INTERNATIONAL, ELECTROTECHNICAL, and COMMISSION, IEC 62271: High-voltage switchgear and controlgear – Part 203: AC gas-insulated metal-enclosed switchgear for rated voltages above 52 kV, vol. 3. 2022.
[6] IEC 60270, "Partial Discharge Measurements," 2015.
[7] INTERNATIONAL, ELECTROTECHNICAL, and COMMISSION, *IEC 62478: High voltage test techniques – Measurement of partial discharges by electromagnetic and acoustic methods*, 1.0. International Standard, 2016.
[8] Robles G, Fresno JM, Martínez-Tarifa JM. Separation of radio-frequency sources and localization of partial discharges in noisy environments. Sensors (Switzerland) 2015;15(5):9882–98.
[9] Alvarez F, Ortego J, Garnacho F, Sanchez-Uran MA. A clustering technique for partial discharge and noise sources identification in power cables by means of waveform parameters. IEEE Trans Dielectr Electr Insul Feb. 2016;23(1):469–81.

[10] Cavallini A, Montanari GC, Contin A, Puletti F. A new approach to the diagnosis of solid insulation systems based on PD signal inference. IEEE Electr Insul Mag 2003; 19(2):23–30.
[11] Ardila-Rey JA, Rojas-Moreno MV, Martínez-Tarifa JM, Robles G. Inductive sensor performance in partial discharges and noise separation by means of spectral power ratios. Sensors (Switzerland) 2014;14(2):3408–27.
[12] W.G. 21.03, "Recognition of Discharges," *CIGRE Electra*, vol. 11, pp. 61–98, 1969.
[13] Zhang H, Zhao T, Liu H, Wang W, Gong W. An anti interference technology of UHF PD detection in UHV GIS based on automatic time difference analysis. Int Conf Adv Electr Equip Reliab Oper AEERO 2021 2021,:1–5.
[14] Mier C, Mor AR, Vaessen P. Design and characterization of a magnetic loop antenna for partial discharge measurements in gas insulated substations. IEEE Sens J 2021;21(17):18618–25.
[15] Mier C, Rodrigo Mor A, Castro L, Vaessen P. Magnetic and electric antennas calibration for partial discharge charge estimation in gas-insulated substations. Int J Electr Power Energy Syst 2022;141(January):108226.
[16] Mier C, Rodrigo Mor A, Vaessen P, Lathouwers A. Magnetic and electric antennas synergy for partial discharge measurements in gas-insulated substations: Power flow and reflection suppression. Int J Electr Power Energy Syst 2023;144(January 2023):1–9.
[17] Kularatna N, Ross AS, Fernando J, James S. Background to surge protection. Des Transient Prot Syst 2019:1–15.
[18] Sack K, Su CQ. A non-contact directional sensor for partial discharge measurements. Conf Rec IEEE Int Symp Electr Insul 2010:1–4.
[19] Rodrigo-Mor A, Muñoz FA, Castro-Heredia LC. Principles of charge estimation methods using high-frequency current transformer sensors in partial discharge measurements. Sensors (Switzerland) 2020;20(9):pp.
[20] Mier C, et al. Methods for partial discharge calibration in gas-insulated substations for HVDC power grids and charge evaluation uncertainty. IEEE Sens J 2023;23(19): 23486–93.
[21] C. Mier, A. Rodrigo Mor, P. Vaessen, "A directional coupler for partial discharge measurements in gas-insulated substations," Measurement: J. Int. Measure. Confeder., vol. 225, 2024. doi: 10.1016/j.measurement.2023.113996.
[22] Gao W, Ding D, Zhao D, Liu W. Propagation properties of high-frequency electromagnetic wave through typical in-field GIS structures. IEEE Trans Power Deliv 2014;29(6):2476–84.
[23] M. Rostaghi-Chalaki, K. Yousefpour, J. Klüss, M. Kurum, J. P. Donohoe, C. Park, "Classification and comparison of AC and DC partial discharges by pulse waveform analysis," *Int. J. Electr. Power Energy Syst.*, vol. 125, no. September 2020, p. 106518, 2021.
[24] Jianqing Wang, O. Fujiwara, K. Sasabe, "A simple method for predicting common-mode radiation from a cable attached to a conducting enclosure," in *APMC 2001. 2001 Asia-Pacific Microwave Conference (Cat. No.01TH8577)*, vol. 3, pp. 1119–1122.
[25] Mier Escurra C. Dataset: Interference. Mendeley Data 2023;1.
[26] C.W. 33/23.12, "Insulation Co-ordination of GIS: return of experience, on site tests and diagnostic techniques," *Electra*, vol. 176, pp. 67–97, 1998.